Cement & Concrete Composites 32 (2010) 281–290

Contents lists available at ScienceDirect

Cement & Concrete Composites

journal homepage: www.elsevier.com/locate/cemconcomp

Analysis of compressive fracture of three different concretes by means of 3D-digital image correlation and vacuum impregnation

Daniel Caduff, Jan G.M. Van Mier *

Institute for Building Materials ETH Zurich, 8093 Zurich, Switzerland

ARTICLE INFO

Article history:
Received 12 August 2009
Received in revised form 6 January 2010
Accepted 20 January 2010
Available online 25 January 2010

Keywords:
Concrete
Fracture
Uniaxial compression
3D-digital image correlation
Vacuum impregnation
Crack orientation

ABSTRACT

Fracture of three different concretes under uniaxial compression was investigated. The three different materials were normal concrete, high strength concrete and foamed cement, with uniaxial strength varying between 8 and 92 MPa. The prismatic specimens were loaded between two different types of loading platens, providing maximum boundary restraint (rigid steel platens) or almost zero boundary restraint (Teflon (PTFE) sandwich inserts). Fracture propagation was measured using 3D-digital image correlation where emphasis was placed on measuring crack development just before and at peak stress. The stress at first cracking is dependent on the resolution of the digital image correlation technique, and as such not very well defined. The frictional restraint of the loading platens is recognized in the failure modes, in particular in the direction and structure of the main cracks. Also, the results for normal and high strength concrete underscore previous results: high friction results in a higher uniaxial compressive strength. This finding was not confirmed for foamed cement, where both loading systems gave approximately the same compressive strength. Likely the Teflon inserts do not function properly on the highly porous surfaces of the foamed cement specimens. The direction of the main cracks at peak is defined before the softening regime is entered: cracks have a vertical orientation when loading is applied through Teflon inserts, whereas 'en-echelon' tensile cracks forming inclined shear bands are observed for rigid loading platens. The results from 3D-digital image correlation were confirmed by results from vacuum impregnation with fluorescent epoxy after test termination. Although digital image correlation is capable of showing cracks at relatively early stages of loading, the vacuum impregnation technique shows all the fine detail and crack branches, but this can, unfortunately, only be done once for each specimen. Therefore, combining the two different techniques is more appropriate.

1. Introduction

Compressive fracture of concrete remains an elusive phenomenon. One of the main problems in studying fracture is that when crack size approaches that of the specimen (or structure), boundary effects, influences of specimen size and the fracture properties become closely interdependent and are difficult if not impossible to separate. This problem has not been resolved to date, in particular not for fracture of cohesive frictional materials like concrete, where fracture is not characterized by the nucleation and growth of a single macroscopic crack, but where in some stages of the fracture process a multitude of small short microcracks appear. The fracture process in compression can be divided into four different stages [1,2] as follows: (O) linear elastic stage, (A) microcracking, (B) macrocrack growth and (C) bridging and frictional restraint. Stages (O) and (A) are associated with the rising branch of the stress–strain curve leading to maximum stress; stages (B) and (C) are related to the degradation of the specimen in the post-peak softening regime. In stage (O) it is assumed that no damage occurs and the material behaves linear-elastic. This is an assumption because due to the manufacturing process of concrete early damage is almost unavoidable, and a truly linear regime will not exist. When external load increases local (tensile) stress concentrations cause the development of small microcracks that can still be arrested by stiffer and strong elements in the heterogeneous material structure. However, upon increasing external load, at some moment the material structure cannot arrest further crack propagation and localization of damage in a single (few) large crack(s) occur(s). We enter stage (B) of the aforementioned fracture process. The carrying capacity of the specimen (or rather structure) is decaying rapidly, and some residual carrying capacity remains due to bridging and frictional interlock in the macrocracks (stage (C)). Macrocrack propagation (stage (B)) is affected by boundary conditions and specimen size and shape, and must thus be seen as a structural property. Bridging (stage (C)) is affected by material composition. For example the size of the largest aggregates as well

* Corresponding author.
E-mail addresses: caduffd@ethz.ch (D. Caduff), jvanmier@ethz.ch, jvanmier@x-s4all.nl (J.G.M. Van Mier).

0958-9465/$ - see front matter © 2010 Elsevier Ltd. All rights reserved.
doi:10.1016/j.cemconcomp.2010.01.003

as the strength and stiffness contrast of the aggregate and matrix define the width of the localized shear-band in compression, and thus the residual stress in the softening regime. All these matters have been presented in detail in the aforementioned papers, and will not be further debated here. The intention of the present paper is to further investigate the damage patterns in different types of concrete subjected to uniaxial compression. Of particular interest is the transition from the microcrack stage (A) to the macrocrack stage (B), which happens around peak stress. Identifying the conditions under which the localized macrocrack(s) nucleate and grow is of great importance for engineering new concretes with improved fracture behaviour and for predicting the failure strength of concrete structures.

Modeling the fracture process is possible using micromechanics, starting from the particle level of concrete (see for example [3–12]). From these microscopic models, all the four aforementioned stages in the fracture process follow directly. The models are usually based on a limited number of well understood and physically-based parameters. Although these models are computationally expensive, they do not suffer from the problem encountered in cohesive fracture models in the spirit of the Fictitious Crack Model [13], and the extension to compressive fracture, [14]. In such models the post-peak regime, i.e. the softening curve is assumed to be a material property in-spite of the un-deniable strong boundary and size effects. In principle testing infinitely large specimens would be required to extract the parameters needed in cohesive crack models, but this runs rapidly into practical problems. Testing 2-(m) large plain-concrete specimens is already a major effort in the best-equipped laboratories in the world [15].

In the present investigation three different concretes of varying quality (defined according their uniaxial compressive strength) and two different boundary conditions were tested. Prismatic specimens were subjected to uniaxial compression between either rigid steel loading platen (the usual standard loading condition in compression tests) or between Teflon (PTFE) friction-reducing pads (as defined by RILEM TC 148 [16]). Thus, the two boundary conditions are 'high frictional restraint' and 'low frictional restraint', which is known to have a significant effect on the failure mode and fracture strength in compression [17]. The three concretes tested were a normal-strength concrete (35–40 MPa), a low-strength foamed cement (8–10 MPa) and a high strength fibre-reinforced concrete (90–95 MPa), which span a large range in behaviour from brittle to quasi-brittle to quasi-ductile. The development of cracks was followed in real time using a 3D-digital image correlation tool (VIC-3D), which allowed monitoring simultaneously two side surfaces of a prism under load. At the end of each test the specimens were subjected to vacuum impregnation, a well-proven method that allows for quite detailed crack detection in the samples. Since this is a destructive method, it can only be used for comparison with the VIC-3D analysis at the end of each experiment.

The paper has been organized as follows. After a brief summary of the used materials and specimen manufacturing methods, the digital image correlation method is explained in some detail. Next the results are presented, in particular the fracture patterns from the VIC-3D measurements in relation to the measured load–displacement curves. The crack patterns from VIC-3D are compared to those from vacuum impregnation in the last load-step. Finally the results are discussed and compared to results from others and conclusions are drawn.

2. Materials and specimens

Uniaxial compression tests were carried out on prisms with a height/diameter ratio of 2. The specimens were cast horizontally in steel moulds of size $280 \times 70 \times 70\ mm^3$. After 24 h the specimens were de-moulded and for the next 34 days cured in a climate room ($T = 20\ ^\circ C$ and RH = 95%). The specimens were cut and ground after 7 days to the required slenderness of 2. Three sides of each specimen were ground, namely the two surfaces that were viewed with the VIC-3D system, and the casting surface. In order to avoid problems with the VIC-3D system larger pores at the viewed surface were filled with a liquid cement suspension. The effect of filling these larger pores can be seen from Fig. 1. After filling the pores, the viewed surfaces were coated with a white paint and sprayed with black aerosol to produce the required surface condition for the digital image correlation.

Three different concretes were tested. Characterized by their compressive strength they covered the entire spectrum from high to very low strength. The expected fracture behaviour was from brittle to quasi-brittle to quasi-ductile. Table 1 shows the three concrete compositions. The foamed cement was produced following the procedure outlined in Meyer et al. [18]. The high strength concrete contained some PVA fibres (Kuraray; 12 mm long, 0.2 mm diameter) and air-entrapping agent to prevent extreme brittle (explosive) failure behaviour and possible damage to the cameras of the VIC-3D system. The maximum aggregate size in the high strength concrete was 4-mm. Normal-strength concrete contained 16-mm river gravel. The ratio D/d_{max} was therefore 70/16, which meets minimum demands for having specimens with a representative volume. Some fresh and hardened concrete properties are listed in Table 2. The compression strength is the average of three tests on prisms ($H/D = 2$) between rigid steel loading platens.

3. Test method and measurement methods

3.1. Loading conditions

The uniaxial compression tests were performed in a Walter + Bai servo-hydraulic testing machine with a capacity of 4000 kN. The loading was applied in force control and the loading rate varied between the three different concretes to ensure that the time to peak-load was the same for each mixture. A load-cell with a measurement range up to 1000 kN was used. For each concrete, three specimens were loaded between rigid steel platens and three specimens were loaded using the friction-reducing Teflon (PTFE) sandwich inserts proposed by RILEM TC 148SSC [16]. For the rigid steel loading platen a 10 mm thick steel platen with exactly the dimensions of the concrete prisms was inserted between the specimen and the machine loading platens. The Teflon sandwich consists of 2 Teflon sheet of 0.10 mm thickness with a 0.05 mm thick grease film in between. The total sandwich was thus 0.25 mm.

Fig. 2 shows the applied loading history for each specimen. It was attempted to increase the force in every cycle without reaching the maximum load the specimen could sustain, except in the last cycle. The last cycle was stopped as soon as a decline in load of 5 kN was measured. At that moment it was assumed that the peak of the stress–strain curve was reached, and that upon further loading the softening regime would be reached.

The whole surface of two sides of each prism was recorded with the two cameras of the digital image correlation system during the 1st and 4th cycle. The image size was 150×150 mm, thus covering the complete specimen length of 140 mm. During the 2nd and 3rd cycles, the upper and lower parts of the two surfaces were recorded separately with an image size of 90×90 mm in an attempt to improve the resolution in (pixel/mm).

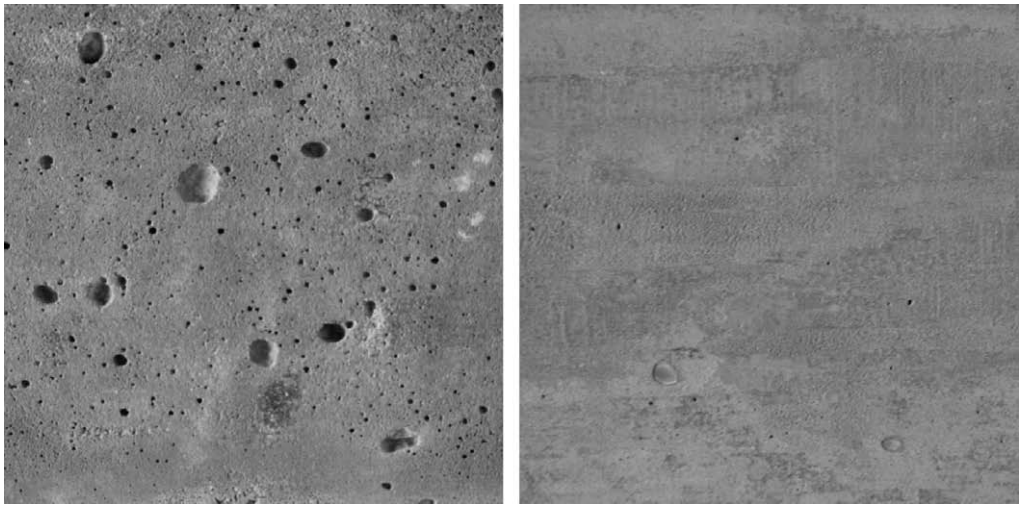

Fig. 1. Same concrete surface without (left) and with (right) filled air voids.

Table 1
Concrete mixture compositions.

Component[a]	Normal concrete	High strength concrete	Foamed cement
Cement type	CEM I 42.5 N	CEM I 42.5 N	CEM I 52.5 R
Cement	344	995	716
Water	155	263	272
0–4 mm sand	953	704	–
4–8 mm aggregate	395	–	–
8–16 mm aggregate	558	–	–
Fly-ash	–	157	–
Micro-silica	–	44	–
Plasticizer (Glenium ACE 30)	–	26	–
Air-entraining agent	–	10	–
PVA fibres	–	26	–
Protein foam	–	–	40

[a] All quantities in kg/m^3.

Table 2
Fresh and hardened concrete properties.

Component	Normal concrete	High strength concrete	Foamed cement
Slump flow (cm)	42	96	–
Small slump flow (cm)	–	–	15.5
Density (kg/m^3)	2362	2278	1013
f_c (MPa)	92.1	37.0	8.5

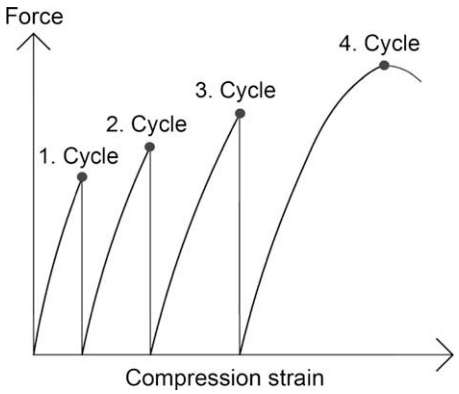

Fig. 2. Loading history for the tested specimens.

3.2. 3D-digital image correlation

The digital image correlation system used was the VIC-3D system provided by LIMESS. 3D-digital image correlation is based on both digital image correlation [19,20] and stereovision, and was developed at the end of last century (see [21–24]). The correlation scores are computed by measuring the similarity of a fixed sub-set window in the first image (reference image on the unloaded specimen) to the shifting sub-set window in the second image (of the loaded specimen). A summary of the algorithm can be found in [25].

The main components of the system used are the two CCD cameras with a resolution of 2048 × 2048 pixels. The cameras are fixed on a traverse in vertical position as indicated in Fig. 3. The cameras can be equipped with lenses of varying focal length, and it is possible using the same system to record the displacements of surfaces of a few millimeters to several meters.

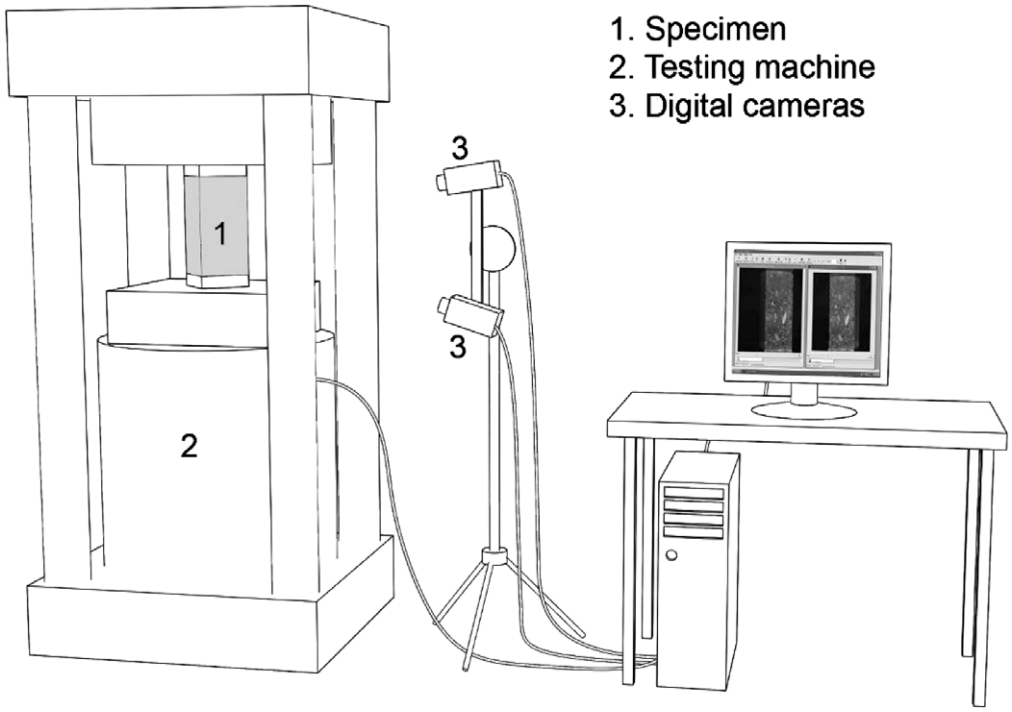

Fig. 3. Setup of the VIC-3D camera in front of the loading rig. The orientation of the specimen allowed viewing two surfaces of a prism simultaneously. The two cameras were placed vertically, as shown.

The actual dimensions of the images depend on the used lens and the distance between the lens and the recorded surface. The angle between the two cameras must be greater than 30°; otherwise the out-of-plane displacement is calculated with a rather poor accuracy. Calibration of the system is essential in order to determine the best possible position of the two cameras, whereas the quality of the calibration also determines the accuracy of the digital image correlation.

As mentioned, for calculating the displacements with digital image correlation a reference image (at zero-load) and an image after deformation must be recorded. Before the software VIC-3D calculates the displacements between these two images an Area Of Interest (AOI) has to be set on the reference image (see Fig. 4). Three parameters affect the displacement and strain calculation, namely the sub-set size, the grid step-size and the strain window size (also called the neighboring matched points). The effects of varying these parameters on the displacement and strain calculation are explained in Robert et al. [25].

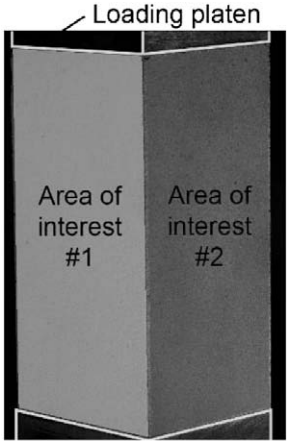

Fig. 4. Location of two Area's Of Interest (AOI) on the recorded image of the specimen.

It should be mentioned, that the image noise cannot be eliminated completely. The magnitude in (mm) for displacement (or in (%) for strain) of the image noise depends on the resolution in (pixel/mm) for the same parameter setting. Therefore, the image noise has a constant value in (pixel) for constant parameter settings while varying the resolution.

In summary of Robert et al. [25], the measuring accuracy improves with increasing values of the three parameters. The image noise decreases when these parameters increase. When uniform displacements are measured, the parameter sizes have no influence on the mean values of the displacements and the strains over the AOI. However, the situation changes when a material like concrete is considered. The displacement fields become very irregular, especially during crack propagation. In order to detect the irregularities, the parameters should be set as small as possible. Small strain concentrations might indicate where cracks nucleate and grow. The obvious problem is the increasing image noise, which may be circumvented by decreasing the size of the image section. This of course has the disadvantage that not the fracturing of the entire specimen can be observed in a single image. If the ratio in (pixel/mm) is increasing when the image section is scaled down, and the image noise is independent of the magnification, then the image noise in (mm) becomes smaller (assuming that the values of the three parameters are identical during the calibration of the displacements and strains in both cases).

To verify the above an image section of size 240 × 240 mm from a surface of a concrete prism was recorded during a compression test. The test was terminated after reaching a load of 600 kN, which is about 93% of the maximum stress for this particular specimen. After un-loading, the specimen was loaded again till 600 kN but the image section was reduced to 120 × 120 mm. In Fig. 5 the principal strains are compared. The background color relates to the value of the image noise, which has the same value in (pixel) for both

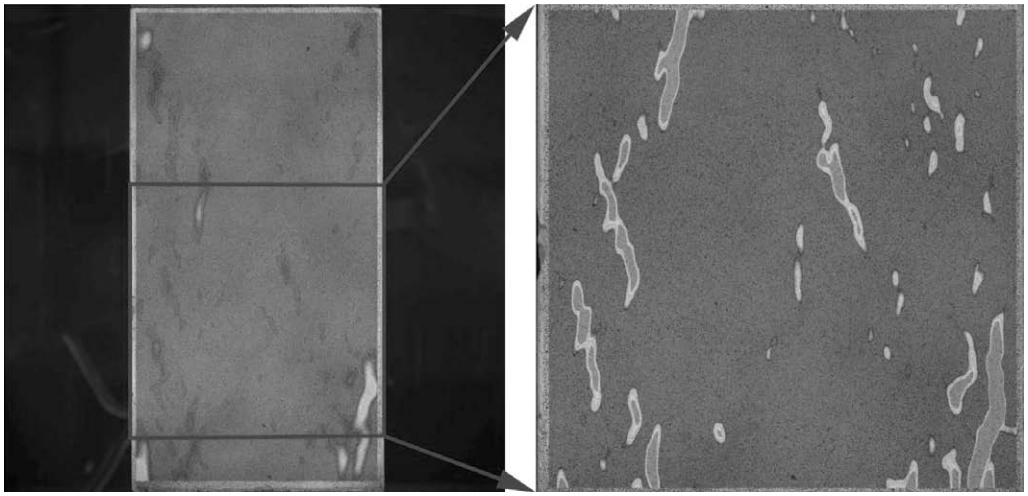

Fig. 5. Comparison of the crack pattern on the surface of a concrete prism loaded to 600 kN using an image size of 240 × 240 mm (left) and 120 × 120 mm (right). Note that the higher resolution image was made after un-loading and re-loading the specimen for a second time to the original loading of 600 kN.

image sizes. The correlation parameters were the same for both calculations. In the large image the shapes of the cracks are not very well reproduced (i.e. are hard to distinguish from the image noise) and the crack widths are over-estimated. With reduced image-section-size cracks are more clearly visible, at smaller crack widths and the crack shape seems better preserved. The dimension of the image section has thus an influence on the stress-level where first cracking is detected and cracks can be separated from the image noise.

A number of other factors have influence on the accuracy of the displacement measurement. When the light conditions are changed during recording, the correlation function calculates the wrong displacements because the shifting sub-set windows cannot be detected correctly. Vibrations and movements of the system during recordings also results in erroneous displacement values. The correlation function malfunctions in regions where the surface has rough edges. Therefore in the present experiments the AOI was kept away from the specimen edges, i.e. was not located at the intersection of the specimen and the background (see Fig. 4).

There are also some advantages of working with a full 3D system. In comparison to working with two-dimensional correlation software, with 3D DIC the surfaces of the specimen do not have to be planar, and the cameras need not to be positioned perpendicular to the observed surface(s). More than one surface of a specimen can be recorded at the same time. With a 3D-system every movement in 3D-space can be measured and the out-of-plane deformation of a surface does not lead to errors in the calculation.

4. Results

In this section the results from the experiments are summarized. After a brief overview of the stress–strain curves of the three different concretes and the determination of the stress-level at first cracking, difference in fracture behaviour between the three different concretes as seen with the 3D-digital image correlation are presented. The specimens were subjected to vacuum impregnation after the last loading cycle, and the crack patterns from the impregnated samples are compared to the digital image correlation results.

4.1. Stress–strain curves

In the first and fourth loading cycle (see Fig. 2), the stress–strain curves of the tested concretes could be determined because the surface strains from two sides of a prism were measured with the digital image correlation system with an image size of 150 × 150 mm. To calculate the axial and lateral strain, a release window was chosen in the middle of the prism with a height of 70 mm. The average axial and lateral strains were calculated over the area of the release window. A typical stress–strain curve for foamed cement is shown in Fig. 6. The ascending branch of the axial strain is linear up to a level of about 30% of peak stress. Initially the lateral strains are of the same order of magnitude as the image noise, and the lateral strain curve is not quite smooth. This effect is reinforced when the volumetric strain is plotted ($\varepsilon_{vol} = \varepsilon_{axial} + 2\cdot\varepsilon_{lateral}$). Obviously the Poisson's ratio, the Young's modulus and the specimen's volume change can be derived directly from the digital correlation data.

In Fig. 7 the stress–strain curves from the first loading cycle are shown for all concretes tested. All test results lie between the two curves shown for each concrete type. The initial modulus for normal concrete and for high strength concrete lies within the same range. The modulus for foamed cement is clearly much lower (see also Fig. 8a). The strength differences are obvious, where it should be recalled that in the first cycle specimens were not loaded to peak stress. In the experiments it was found that the differences

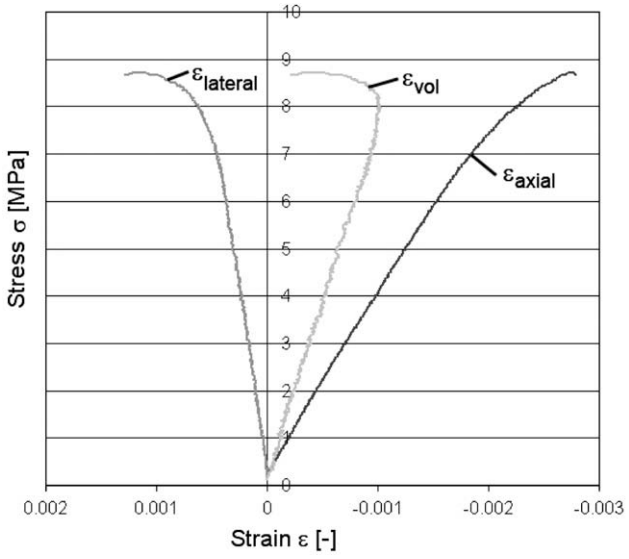

Fig. 6. Stress–strain curve, measured during the 4th cycle.

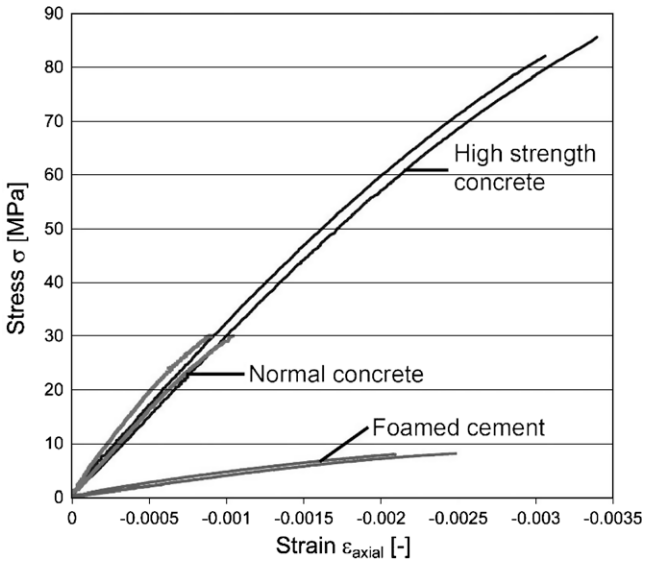

Fig. 7. Enveloping curves of the axial strain for all mixtures.

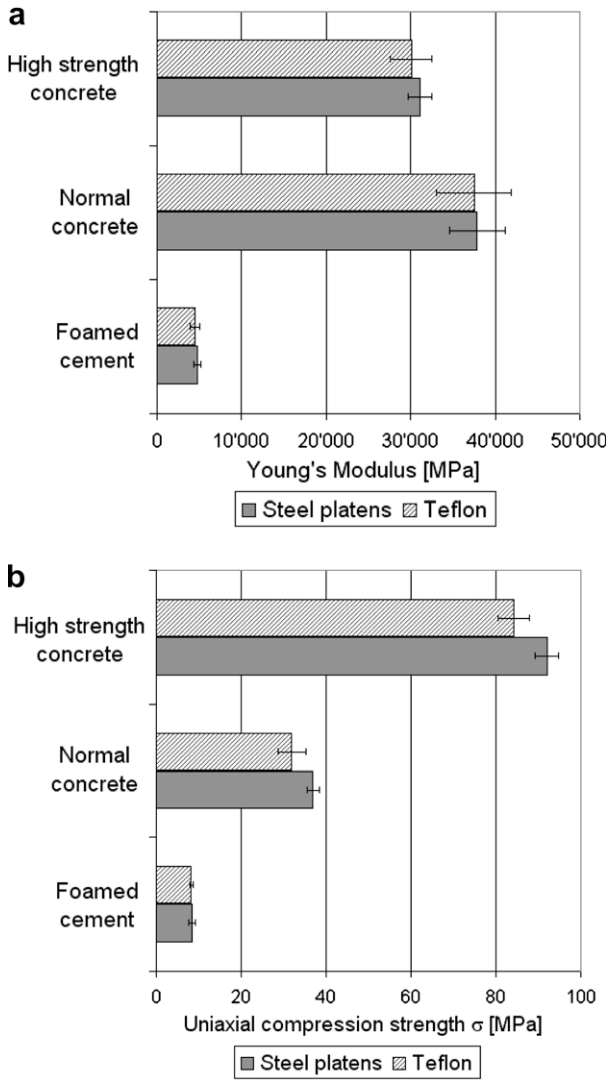

Fig. 8. (a) Young's modulus for the three mixtures: results from tests between rigid steel platens and Teflon platens are shown separately. (b) Effect of loading platen on the uniaxial compression strength for three different concretes tested.

in this initial part of the ascending part of the stress–strain curves was not different when either rigid steel loading platens or Teflon friction-reducing pads were used.

In Fig. 8 the measured Young's modulus in the first loading cycle and the maximum compressive strength for the three concretes, loaded between rigid steel platens and Teflon inserts are gathered. The Young's modulus of the high strength concrete is lower than that for the normal concrete because it contains no rough aggregates. Foamed cement has a much lower Young's modulus than the two other concretes, which is caused by the large air content and the aggregate content of the normal concrete is higher. Differences between loading system on Young's modulus are small and negligible. Note that the scatter band for the Teflon inserts is relatively large, especially for the normal concrete and the high strength concrete. The uniaxial compressive strength is clearly more affected by the boundary restraint exerted by the loading platens, and confirms experiments by others. Surprising is that for foamed cement the differences between rigid steel platens and Teflon inserts decreases substantially, and it can be concluded that the loading platen friction has no influence on the strength of foamed cement.

4.2. Stress at first cracking

In Table 3 are listed the mean value and the standard deviation of the stress (as percentage of the peak stress) at first crack observation for the four load cycles. No distinction is made between concretes, or between loading condition (low and high frictional restraint) because the observed differences were very small. The stress-levels are normalized to the peak stress for every specimen to allow for comparison of results. Beginning at the 1st load-cycle, the first crack is observed at an average stress of 71% with a standard deviation of 8%. The stress-level drops to 44% in the second load-cycle. This is not only caused by increasing damage in the specimen, which would decrease the stress at which crack propagation continues, but also because the recorded image section is reduced (see Section 3.1). The reduction of the image size increases the resolution in (pixel/mm) and also the measurement accuracy. Between the 2nd and 3rd cycle the results can be compared directly since the image size has not been changed. Between the 3rd and 4th cycle the stress-level at first cracking increases again since the image size was brought back to the original size at the first cycle. Comparing the results of the 1st and 4th cycle shows that the first crack level decreased from 71% to 44%. This is directly the result from the three additional load-cycles. These results are in agreement with earlier observations of concrete loaded to cyclic compression; see for example in Van Mier [26].

4.3. Digital image correlation

The following images were recorded at the peak of the 4th cycle for each specimen. The settings of the parameters in the VIC-3D system were the same for every analysis, with a sub-set of 21, a step size of 5 and a strain window size of 5. The largest maximum

Table 3
Comparison of stress-level at first crack.

	Stress level as percentage of peak stress (%)	
	Mean value	Standard deviation
1st cycle	70.56	8.02
2nd cycle	44.44	9.84
3rd cycle	36.88	14.01
4th cycle	43.53	16.56

principal strain is indicated by white. In interpreting these results one has to be careful since the maximum principal strains do not have the same value in all images. The image noise lies between 0.10% and 0.15% for the used parameter settings. It is assumed that every visible strain concentration indicates a crack.

Fig. 9a and b shows the cracking in two normal concrete prisms loaded between high friction boundary conditions and low friction boundaries respectively. Steel platens were used in Fig. 9a. Two global 'shear-bands' can be identified on the two recorded surfaces of the prism. The 'shear bands' (inclined cracks) extend over the entire height of the specimen. The 'shear bands' appear to consist of vertical splitting cracks. The cracks with the largest principal strains have a vertical orientation; cracks with a more inclined orientation in general show smaller principal strains. Cracks seem to propagate from the specimen's corner only; along the edges hardly any further cracks were found, which may be the result of the high friction end condition. In Fig. 9b the crack patterns obtained from a test on normal concrete loaded between Teflon inserts is shown (low friction). In the normal concrete specimens large air voids were not filled with the liquid cement suspension, and the effect is directly visible. High principal strains are calculated at the location of the air voids, but luckily due to their round shapes the air voids can easily be distinguished from the cracks. In this test vertical splitting cracks were detected on the left surface. The cracks did not appear to 'line-up' in a 'shear band' as 'en-echelon' tensile cracks. Moreover cracks not only propagate from the corners but also along the edge (see the right surface, along the bottom). This may be a direct consequence of the low friction boundary condition.

The high strength concrete prism, loaded between stiff steel platens, is shown in Fig. 10a. The behaviour is quite comparable to that of the normal concrete in Fig. 9a. In particular on the right surface the shear band seems to manifest itself in the same way as in the normal concrete prism. The shear band does not extend over the full height of the specimen, but is composed of a number of vertical splitting cracks. The black region on the top side of the right surface, near the main crack is the result of spalling. The VIC-3D software automatically ignores this region. The high strength concrete specimen loaded between Teflon shows a number of vertical splitting cracks, mostly along the top side of the specimen (Fig. 10b). The longest cracks propagate almost over the length of the specimen;

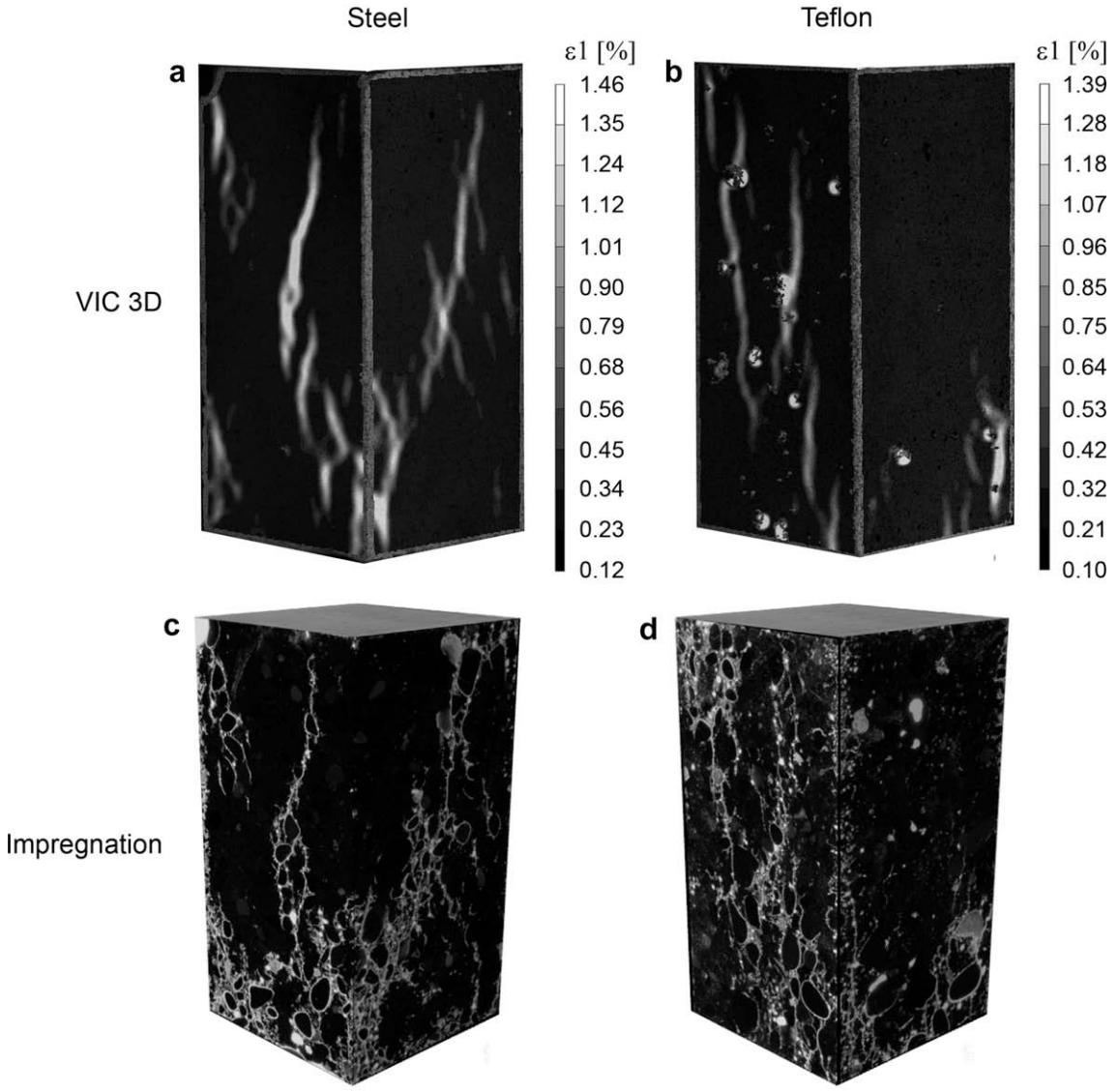

Fig. 9. Crack patterns in a normal concrete at peak-load of cycle 4: (a, c) loaded between rigid steel platens and (b, d) loaded between Teflon. Figures a and b show the strain concentrations visualised with digital image correlation; figure c and d shows crack patterns after vacuum impregnation.

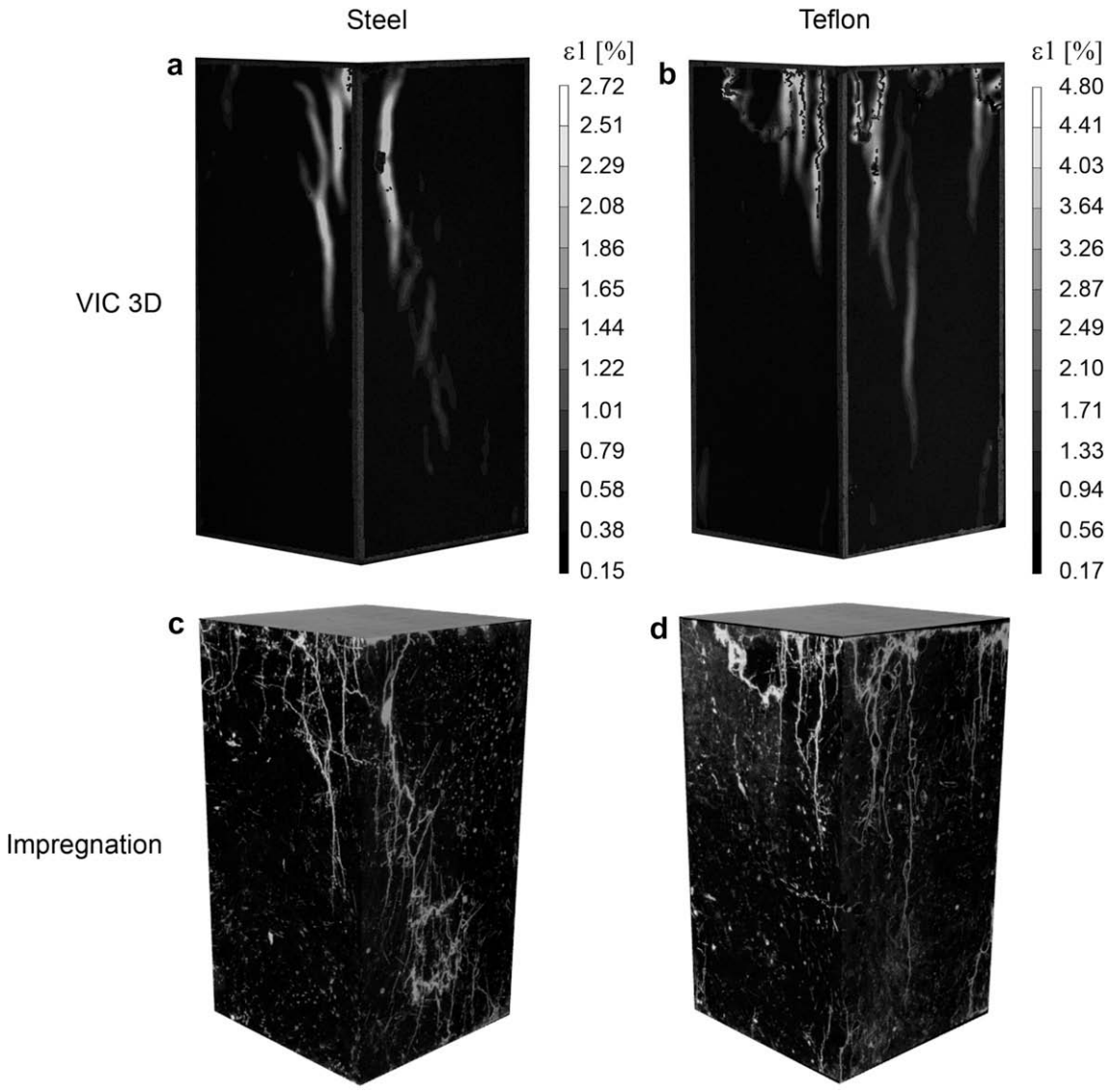

Fig. 10. Crack patterns in high strength concrete at peak-load of cycle 4: (a, c) loaded between rigid steel platens and (b, d) loaded between Teflon. Figures a and b show the strain concentrations visualised with digital image correlation; figure c and d shows crack patterns after vacuum impregnation.

the largest cracks widths are found near the loading platens. The friction is obviously quite effectively reduced by means of the Teflon inserts.

In the foamed cement specimen loaded between steel platens a large inclined crack runs over the left surface (see Fig. 11a). A second inclined crack, a shorter one, develops from the left top corner, and grows towards the major inclined crack on the left surface. On the right surface cracks also develop from the corners, and take an inclined orientation. The cracks are probably not 'shear bands' as observed in the normal concrete specimens, and are just inclined large cracks and not built-up as 'en-echelon' tensile cracks. When low friction boundaries are applied, Fig. 11b (Teflon), the cracks take a more vertical orientation and do not only initiate from the corners of the specimen. Nevertheless, the main crack seems to develop from a corner, i.e. the left top of the right surface, which might indicate that the Teflon pads do not function properly between a steel platen and a porous foamed cement surface. The triangular confinement area as develops in the foamed cement specimen loaded between steel platens (Fig. 11a, top of left surface) is however not observed in the foamed cement sample loaded between Teflon inserts.

4.4. Vacuum impregnation

The six prisms that were shown in Figs. 9–11 were selected for vacuum impregnation with a fluorescent epoxy dye that allows for high-resolution crack detection under ultra-violet light. The technique was originally developed by Vonk [4] for crack detection in confined specimens loaded in compression. Over the years the technique has become a standard procedure to establish crack patterns in a variety of tensile, shear and compressive fracture experiments (for a description of the current, modified version of the technique, see Stähli [27]). After impregnation the surfaces of the specimens were ground until all excess epoxy was removed. The same surfaces that were observed with the digital image correlation system were photographed under ultra-violet light after impregnation, and the results are also gathered in Figs. 9–11, below the results from the digital image correlation for easy comparison.

For normal concrete the crack patterns are shown in Fig. 9c and d for steel and Teflon inserts respectively. The specimen loaded between steel platens shows the same shear bands, which, as now can clearly be seen, are built-up from vertical cracks with

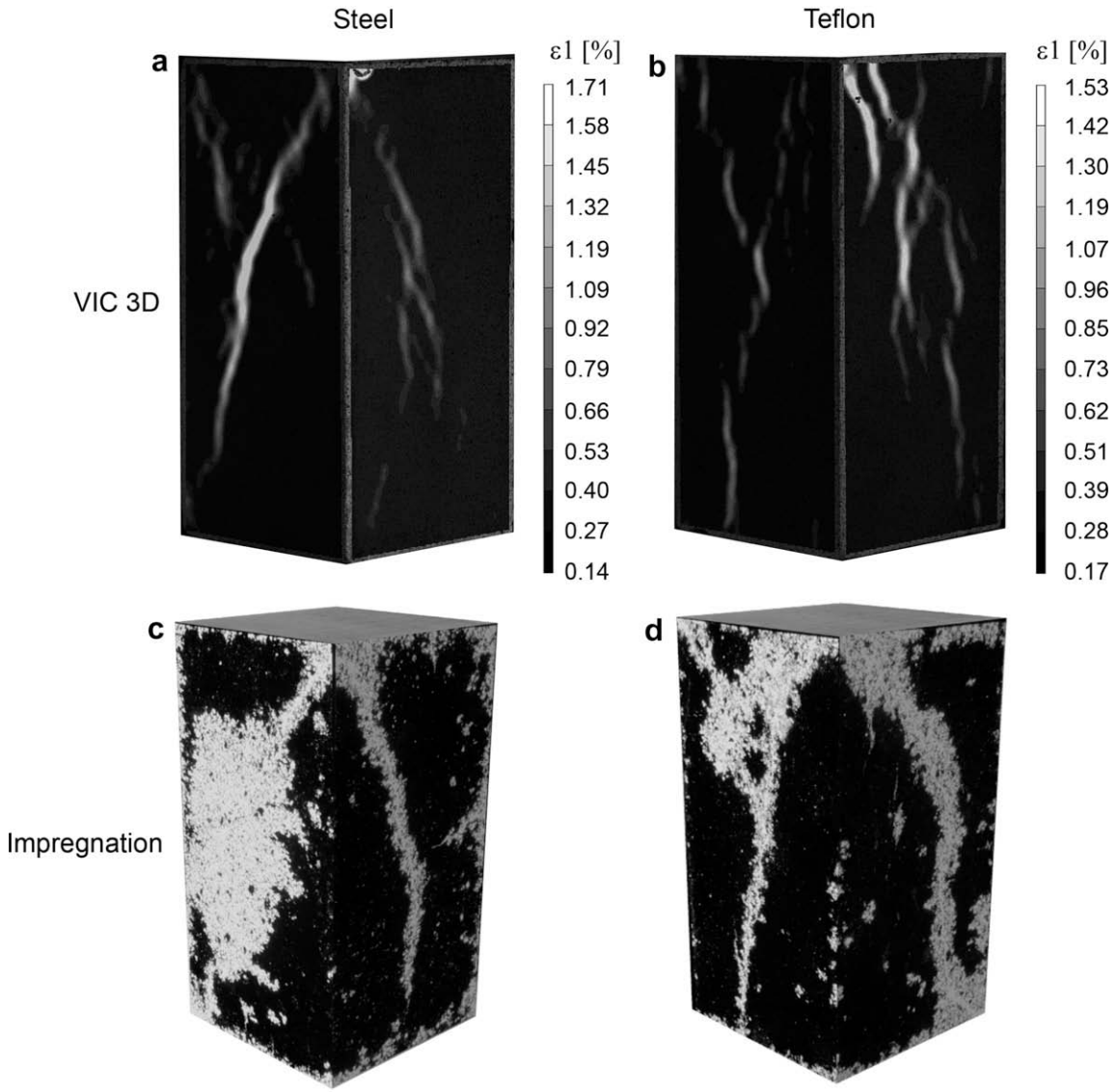

Fig. 11. Crack patterns in foamed cement at peak-load of cycle 4: (a, c) loaded between rigid steel platens and (b, d) loaded between Teflon. Figures a and b show the strain concentrations visualised with digital image correlation; figure c and d shows crack patterns after vacuum impregnation.

'horizontal' connections. The 'horizontal' cracks are located between matrix and aggregates where a weak interfacial transition zone is present characterized by a higher porosity than the bulk cement matrix [28]. As can be seen, the crack patterns from impregnation correspond quite well to the cracks detected with the digital image correlation (compare to Fig. 9a and b for normal concrete). Only the global crack patterns are visible with VIC-3D, and all the tiny detail is lost because of insufficient resolution. For example, quite often when two cracks run more-or-less parallel, the VIC-3D measurement will show only a single crack. For the specimen loaded between Teflon, the correspondence between the digital image correlation measurement and the impregnated specimen is quite satisfactory, be it, of course that the impregnation shows much more fine detail.

The same observations can be made for the high strength concrete: the impregnation shows much more fine detail than the digital image correlation can possibly produce (compare Fig. 10a and c and Fig. 10b and d for steel and Teflon platen respectively).

Figs. 11c and d show the impregnated foamed cement specimens, again for steel and Teflon inserts. Another difficulty with the highly porous foamed cement is that the bubble structure is also impregnated and cracks are hard to distinguish. For this material the VIC-3D approach seems superior, in-spite of the lower resolution. With the foamed material removing a sufficiently thick surface layer seems important. In Fig. 11c the left surface should be ground down further in order to reveal the cracks better, like on the right surface. However, when too much material is removed it becomes difficult to compare the location of cracks detected with both measurement methods.

5. Discussion and conclusions

The experiments confirm trends that have been observed in compression tests on concrete in the past. The foamed cement behaves a bit different, and the use of friction-reducing pads appears to be less useful. It appears that the soft Teflon sandwiches are pressed into the porous material, and are obviously less effective. For foamed cement it could be argued that a low friction insert would be very important because of the low Young's modulus of the material (max 5 GPa, see Fig. 8a). For normal and high strength concrete the present tests are in agreement

with earlier observations, for example those made in the extensive Round Robin performed by RILEM TC148SSC [29].

Interesting is that already in the pre-peak regime of the stress–strain diagrams major regions of high strain can be observed with the digital correlation technique. The images shown in Figs. 9–11 are taken at the maximum load-level of cycle 4 (see Fig. 2), and it seems that crack directions are fixed already in this stage of the experiment. The frictional restraint of the loading platens has influence on the inclination of the main cracks. With low friction cracks tend to run in vertical direction, i.e. parallel to the compressive loading, whereas a larger inclination is observed when high friction loading platens are used. Van Mier [2] showed that this inclination can be calculated when the friction coefficient between specimen and loading platen is known. Kotsovos [17] showed that with increasing frictional restraint the orientation of cracks at the end of the softening regime increases. The current experiments show that the crack direction is already fixed at peak stress. Therefore, it can be speculated that after peak not much will change, other than that the major cracks will further propagate and widen.

Based upon the results presented in this paper the following conclusions can be drawn:

- The experiments confirm that with the use of friction-reducing pads a lower compressive strength is measured in comparison with tests between rigid steel platens. This is in particular the case for normal and high strength concrete. For foamed cement, the use of Teflon inserts seems not useful for friction reduction and the influence on the compression strength could not be observed.
- RILEM TC148SSC recommends the use of friction reducing measures for the measurement of compressive strength and softening properties of concrete. The present results indicate that for low-strength materials, like the foamed cement, such friction reducing measures are not very useful. The soft Teflon sandwich is pressed into the porous surface of the foamed cement and is therefore less effective.
- For all three concretes cracks have a vertical orientation when specimens are loaded between Teflon inserts, whereas the (main) cracks have a certain inclination when steel loading platens are used.
- The resolution of the measurement technique determines when first cracks are visible. Comparing data from experiments using crack detection techniques with differing resolution is therefore not allowed.
- Digital image correlation can show regions of high strain at very early stages of loading, and growth of the cracks can be followed in real time. The impregnation technique is destructive, and can only be applied at the end of a certain load cycle. Re-loading is thereafter not possible. Nevertheless, with the impregnation technique much of the fine detail in the crack patterns can be visualised.
- From past experience it is known that the inclination of the cracks in the post-peak regime depends on the frictional restraint of the loading platens (e.g. [4,17]). The present experiments show that at peak-load the orientation of cracks is already fixed and dependent on the frictional restraint of the loading system.

Acknowledgements

The authors would like to acknowledge the help of Mr. Dominik Meyer in producing the foamed cement samples, as well as of Mr. Heinz Richer of the concrete lab at the Institute for Building Materials for his help with the various experiments.

References

[1] Van Mier JGM. Framework for a generalized four-stage fracture model of cement-based materials. Eng Fract Mech 2008;75:5072–86.
[2] Van Mier JGM. Mode II crack localization in compressive fracture of concrete. J Eng Mech (ASCE) 2009;135(1):1–8.
[3] Roelfstra PE, Sadouki H, Wittmann FH. Le béton numérique. Mater Struct (RILEM) 1985;18(107):327–35.
[4] Vonk RA. Softening of concrete loaded in compression. Ph.D. thesis, Eindhoven University of Technology, The Netherlands; 1992.
[5] Stankowski T, Sture S, Willam KJ, Runesson K. Simulation of failure processes in cementitious composites – concrete. In: Van Mier JGM, Rots JG, Bakker A, editors. Fracture processes in concrete, rock and ceramics. London: E&FN Spon; 1990. p. 139–48.
[6] Schlangen E. Experimental and numerical analysis of fracture processes in concrete. Ph.D. thesis, Delft University of Technology; 1993.
[7] Schlangen E, Van Mier JGM. Experimental and numerical analysis of the micromechanisms of fracture of cement-based composites. J Cem Concr Compos 1992;14(2):105–18.
[8] Bolander JE, Hikosaka H, He WJ. Fracture in concrete specimens of different scale. Eng Compos 1998;15(8):1094–116.
[9] Wang J, Navi P, Huet C. Application of fracture mechanics to the study of crack propagation in concrete structures using a granular microcracked model. In: Rossmanith HP, editor. Fracture and damage of concrete and rock. London: E&FN Spon; 1993. p. 176–85.
[10] Lilliu G. 3D analysis of fracture processes in concrete. Ph.D. thesis, Delft University of Technology; 2007.
[11] Lilliu G, Van Mier JGM. 3D lattice type fracture model for concrete. Eng Fract Mech 2003;70(7/8):927–42.
[12] Carol I, Idiart A, Lopez CM, Caballero A. Advances in meso-mechanical analysis of concrete specimens using zero-thickness interface elements. In: Carpinteri A et al., editors. Fracture mechanics of concrete and concrete structures – proceedings FraMCoS-6. London: Taylor & Francis Group; 2007. p. 163–74.
[13] Hillerborg A, Modeer M, Petersson P-E. Analysis of crack formation and crack growth in concrete by means of fracture mechanics and finite elements. Cem Concr Res 1976;6:773–82.
[14] Hillerborg A. Fracture mechanics concepts applied to moment capacity and rotational capacity of reinforced concrete beams. Eng Fract Mech 1990;35(1/2/3):233–40.
[15] Van Vliet MRA. Size effect in tensile fracture of concrete and rock. Ph.D. thesis, Delft University of Technology, The Netherlands; 2000.
[16] RILEM TC 148-SSC. Test method for measurement of the strain-softening behaviour of concrete under uniaxial compression: test recommendation. Mater Struct (RILEM) 2000;33:347–51.
[17] Kotsovos MD. Effect of testing techniques on the post-ultimate behaviour of concrete in compression. Mater Struct (RILEM) 1983;16(1):3–12.
[18] Meyer D, Trtik P, Rindlisbacher M, Van Mier JGM, Voide R, Müller R. Preliminary study on the properties of protein foam and hardened foamed cement paste. In: Proc. CONMAT '05 – special symposium sydney mindess 65 years, August 20–23; 2005 (CD-ROM).
[19] Sutton MA, Wolters WJ, Peters WH, Ranson WF, McNeill SR. Determination of displacements using an improved digital correlation method. Image Vision Comput 1983;1:133–9.
[20] Choi S, Shah SP. Measurement of deformations on concrete subjected to compression using image correlation. Exp Mech 1997;37:307–13.
[21] Helm J, McNeill S, Sutton M. Improved three-dimensional image correlation for surface displacement measurement. Opt Eng 1996;35(7):1911–20.
[22] Kahn-Jetter Z, Chu T. Three-dimensional displacement measurements using digital image correlation method and photogrammetric analysis. Exp Mech 1990;30(1):10–6.
[23] Luo P, Chao Y, Sutton M, Peters W. Accurate measurement of three-dimensional deformations in deformable and rigid bodies using computer vision. Exp Mech 1993;30(1):123–32.
[24] Synnergren P, Sjödahl M. A stereoscopic digital speckle photography system for 3-D displacement field measurements. Opt Lasers Eng 1999;31:425–43.
[25] Robert L, Nazaret F, Cutard T, Orteu JJ. Use of 3-D digital image correlation to characterize the mechanical behavior of a fibre reinforced refractory castable. Exp Mech 2007;47:761–73.
[26] Van Mier JGM. Multiaxial strain-softening of concrete. Mater Struct (RILEM) 1986;19(3):179–200.
[27] Stähli P. Ultra-fluid, oriented hybrid-fibre-concrete. Ph.D. thesis, ETH Zurich, Switzerland; 2008.
[28] Zimbelmann R. A contribution to the problem of the cement–aggregate bond. Cem Concr Res 1985;15:801–8.
[29] Van Mier JGM, Shah SP, Arnaud M, Balayssac JP, Bascoul A, Choi S, et al. Strain-softening of concrete in uniaxial compression. Mater Struct (RILEM) 1997;30:195–209.